eJSE International

Special Issue: Electronic Journal of Structural Engineering 13(1) 2013

Structural and Material Characterisation of Insulated Rail Joints

N. Zong[1*], D. Wexler[2], & M. Dhanasekar[1]

[1]*School of Civil Engineering and Built Environment, Science and Engineering Faculty, Queensland University of Technology, Brisbane, Australia*

[2]*School of Civil Engineering and Built Environment, Science and Engineering Faculty, Queensland University of Technology, Brisbane, Australia*

**Corresponding author:* roger.zong@qut.edu.au

ABSTRACT: Insulated rail joints are designed in a similar way to butt jointed steel structural systems, the difference being a purpose made gap between the main rail members to maintain electrical insulation for the proper functioning of the track circuitry at all times of train operation. When loaded wheels pass the gap, they induce an impact loading with the corresponding strains in the railhead edges exceeding the plastic limit significantly, which lead to metal flow across the gap thereby increasing the risk of short circuiting and impeding the proper functioning of the signalling and broken rail identification circuitries, of which the joints are a critical part. The performance of insulated rail joints under the passage of the wheel loading is complex due to the presence of a number of interacting components and hence is not well understood. This paper presents a dynamic wheel-rail contact-impact modelling method for the determination of the impact loading; a brief description of a field experiment to capture strain signatures for validating the predicted impact loading is also presented. The process and the results of the characterisation of the materials from virgin, in-service and damaged insulated rail joints using neutron diffraction method are also discussed.

Keywords: Beam-columns, Joints, Concrete, Steel, Finite element analysis

1 INTRODUCTION

Insulated rail joint (IRJ) is an essential component in track circuitry that controls both the signalling and the broken rail identification systems and hence is regarded as a safety critical element in the track structure design. To ensure electrical insulation, non-conducting components of the IRJs should maintain contact with their neighbouring conducting components within the IRJ assembly. As all components including the rails are steel, they are wrapped and well bonded using electrically insulated fiber mats such that no metal-to-metal surface contact ever occurs.

IRJs are structurally designed in a similar manner to butt joints in steel design, with the only difference being the need to maintain a gap between the two main members (rails) of the assembly. Due to the presence of this purpose made gap between the two rail ends, IRJs are regarded as a structural weak spot. The section modulus of the joint bars (or, fishplates) that connect the two rails is generally two-third of that of the rail, causing higher deformation (relative to the continuous rail, for example) due to passage of loaded wheels across the joint and gap.

Unfortunately, the current design of the IRJ, in spite of being manufactured under high standards of quality assurance in factories, exhibits highly variable service lives with mean life in the order of 20% of the life of the continuously welded rails (CWR) (Davis and Akhtar, 2005). Furthermore, during service track maintenance crews must frequently assesses any potential for metal contact due to metal flow across insulators, failure of the insulators themselves, or damage to other components of the IRJ assembly which may lead to IRJ failure. In the case of metal flow, there are incidences where crews chisel or grind away track in order to remove any overflown metal leading to potential impact zones for subsequent wheel passage. The problem of maintaining the IRJs in their virgin design state thus remains much of a challenge to the rail industries around the world.

Current designs of IRJ are reported to be structurally adequate from a theoretical perspective for the assumed equivalent static wheel loads (calculated as $(1+\phi)P_0$, where ϕ is dynamic load factor and P_0 is static wheel load) provided the support substructure remains firm. Due to the differences in elastic moduli of the insulating materials and the railhead, impact occurs even when well-conditioned wheels pass over the well installed, new IRJs. These impact forces combine with other forces associated with wheel-rail contact because localised damage of IRJs [2]; the damage and impact then forms a vicious circle with the one aggravating the other leading to early failure.

Track systems are conventionally analysed using the beams on elastic foundation theory with the rails modelled as infinite beams resting on uniform elastic foundation, and the wheel loads modelled as a series of concentrated loads moving on the top of the beam. Newton and Clark (1979) studied rail/wheel dynamic interaction based on a model using multiple layers of discretely supported continuous rail beams. Extending the principle of beams on elastic foundation specifically to IRJs, Kerr and Cox (1999) have modelled the rail and the joint bars as elastic beams and the epoxy-fiberglass insulation as spring layers using the Zimmermann hypothesis. Jenkins et al. (1974) studied the dipped rail joints using the rigid body dynamic methods. They modelled the rail joint as a dipped continuous beam supported on spring and dashpot sets at the location of sleeper supports. Steenbergen (2006) presented a multi-point contact model to determine the impact forces at the IRJ; the model required a definition of step or ramp type discontinuity as a priori to simulate the gapped joints. Such models predict static bending stresses and vertical deflections accurately, but are not very useful for local failure predictions.

Few finite element models have been developed to simulate the dynamic stresses near rail joints. Chen et al. (2002, 2003) carried out finite element analyses of IRJs subjected to static vertical wheel loads and longitudinal brake force. They found that the traditional Hertzian contact theory is no longer valid for predicting the contact stress distribution in the vicinity of the rail joints. Wen et al (2005) performed dynamic finite element analysis for the standard fishplate rail joint containing a gap. They employed a coupled implicit-explicit technique for solving the initial steady deformation prior to and during the process of impact. They found that the impact force increased linearly with the increase in the wheel load. When the vertical and lateral alignments remain perfect, the wheel speed appears to have only a minor effect to the impact force compared to the effect of changes in wheel load.

This paper reports a 3D FE modelling and experimental study of the IRJ for the purpose of predicting the contact impact force time series and the accumulated material damage of the railhead close to the edges of the railhead in the vicinity of the joint. The results shown in the rest of the paper provide a better understanding of the behavior of the IRJ under the wheel rolling passage and directions of further optimising the current design. In this paper, a coupled implicit-explicit algorithm is used for the contact impact modelling and a submodelling technique is employed for the prediction of localised railhead damage. The basic formulation for modal analysis and explicit integration scheme is presented in Section 3 and the finite element modelling for contact-impact is described in Section 4. Modal analysis of the rail track system and some limited examples of contact impact analyses are presented in Section 5. A field experimentation and validation of the FE results are presented in Section 6. Section 7 presents details of the characterisation of railhead materials from the field tested IRJs. Section 8 summarises the paper and contains some general and specific conclusions.

2 RAILHEAD-WHEEL CONTACT IMPACT

2.1 The wheel and railhead

The most common profiles of the wheel and the railhead are shown in Figure 1. The wheel profile consists of a flange to guide the trains along the rails and a conical tread that contacts the railhead. The wheel tread – railhead contact occurs at a very small area, typically 150mm2 to 180mm2. The magnitude of the static load that is transmitted by the wheel to the railhead is typically more than 120kN in heavy haul railways with maximums of 150kN. Therefore it can be seen that contact stresses in the range of 1000MPa could be routinely generated even under the static loading. Under dynamic loading, especially when dip weld joints or flat wheels are encountered, impact forces occur. The seriousness of the contact-impact forces that possess high levels of damage potential could thus be realised. In response to these damage potentials, longer life rail technology has recently been developed in Europe as reported by Heinsch (2004). In this technology a more durable material is laser welded to the running surfaces of the railhead. In contrast, the Australian experience of grinding and friction management for improved rail life, with particular attention to heavyhaul rail networks, has been presented in a comprehensive review paper by Marich (2006).

Where actual force generated at the wheel-railhead interface is of interest, patented instrumented wheelset technology (for example, see Higgins et al. (1996)) is used. Instrumented wheelsets use strain gauges along selected locations of the wheelset and use proprietary software to calculate the wheel-rail contact forces in the vertical, lateral and longitudinal directions with precision. At research level in Japan a similar technology is developed as reported by Kenehara and Fujioka (2002) where disk wheels are provided with holes to accommodate strain gauges.

Jonsson et al (1999) has described a theoretical framework for an inverse method of predicting rail-head forces by strain gauging both sides of the rail foot. From the brief review it could be inferred that strain gauging is the most popular method of sensing the wheel-railhead contact forces; either the wheel or the rail are strain gauged. It should be noted that these strain gauge technology ideas are targeted for sensing typical wheel-railhead forces; specific high frequency impacts have not yet been explicitly reported.

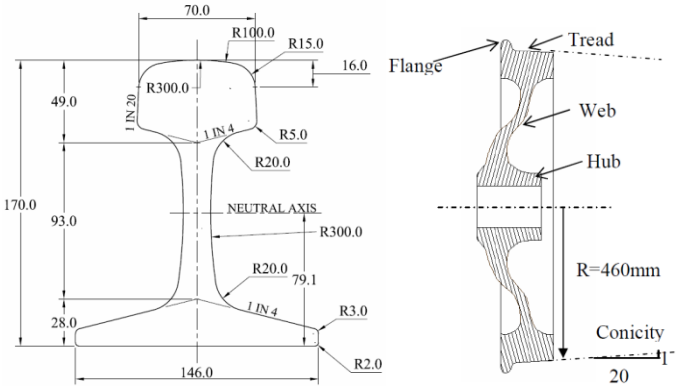

Figure 1: Profiles of rail and wheel

2.2 Mechanics of contact impact

IRJs are designed and installed at site with a view to providing a smooth running surface. Unfortunately the difference in the elastic moduli of the railhead steel and the end post material causes discontinuity with the joint effectively forming a step or ramp as modelled in Steenbergen (2006). The concept is illustrated in Figure 2.

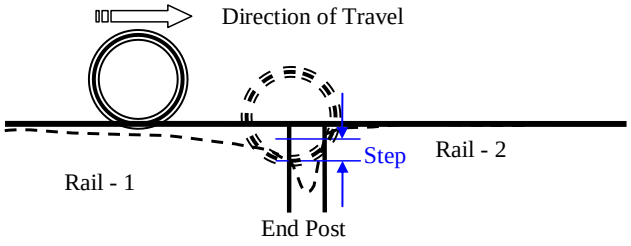

Figure 2: Wheel impact at joint gap

3 REVIEW OF DYNAMIC FE MODELLING

3.1 Modal analysis

Finite element modelling for the extraction of Eigenvalues involves large but usually narrowly banded matrices; the Eigenvalue problem of a finite element model is expressed as shown in equation (1).

$$\left(\mu^2 M + \mu C + K\right)\Psi = 0 \qquad (1)$$

where M is the mass matrix, C is the damping matrix; K is the stiffness matrix; μ is the Eigenvalue; and Ψ is the Eigenvector of the modes of vibration. Lanczos procedure that consists of a set of Lanczos "runs," in each of which a set of iterations is used in the extraction of the Eigenvalues is adopted in ABAQUS/Standard. For each Lanczos run the following spectral transformation is applied:

$$M(K-\xi M)^{-1}M\Psi = \mu M\Psi \qquad (2)$$

where ξ is a shift parameter expressed in the unit of (Length)-1. This transformation allows rapid convergence; in general, only tens of Eigenvalues are computed in a single Lanczos run. After the Eigenvalue of each mode is extracted, the natural frequencies and the corresponding mode shapes are calculated from equation (1).

3.2 Explicit dynamic analysis

A set of approximate nonlinear equilibrium equations for displacement based finite element methods is given in [9]

$$\int_{V_0} B^T \sigma dV_0 = \int_S N^T t dS + \int_V N^T f dV \qquad (3)$$

where σ, t, and f denote the stress, the external traction, and the body force vectors respectively; B and N denote the strain – deformation transformation and the interpolation matrices; V and S denote the volume and surface of the finite body; V_0 denotes the initial volume. For static problems, a system of equations is obtained from (3) for models with *n* elements as follows:

$$\sum_{i=1}^{n}\int_S B_i^T \sigma_i dV_{i0} = \sum_{i=1}^{n}\int_S N_i^T t_i dS_i + \int_V N_i^T f_i dV_i \qquad (4)$$

Representing the left hand side of (4) with I (standing for the global internal force vector) and the right hand side of (4) with E (standing for the global external force vector), the system of equations in equation (4) is schematically represented for static problems as in equation (5).

$$I - E = 0 \qquad (5)$$

For dynamic problems, however, the inertia contribution is also essential and hence (5) is modified as shown in (6).

$$M\ddot{u} + I - E = 0 \qquad (6)$$

where u is the displacement vector; the global consistent mass matrix M is determined using (7).

$$M = \sum_{i=1}^{n}\int_{V_0} \rho_{i0} N_i^T N_i dV_{i0} \qquad (7)$$

in which ρ_{i0} is the reference density of the i^{th} element.

To solve the system of equations (6), the explicit dynamics analysis procedure employs the implemen-

tation of an explicit integration rule together with the use of diagonal element mass matrices. The equations of motion for the body are integrated using the explicit central difference integration rules:

$$\dot{u}^{(j+\frac{1}{2})} = \dot{u}^{(j-\frac{1}{2})} + \frac{\Delta t^{(j+1)} + \Delta t^{(j)}}{2}\ddot{u}^{(j)} \quad (8)$$

$$u^{(j+1)} = u^{(j)} + \Delta t^{(j+1)}\dot{u}^{(j+\frac{1}{2})} \quad (9)$$

where $\dot{u}$ is velocity vector and $\ddot{u}$ is acceleration vector. The superscript j refers to the increment number and $(j-\frac{1}{2})$ and $(j+\frac{1}{2})$ refer to mid increment values. The central difference integration operator is explicit in that the kinematic state can be advanced using known values of $\dot{u}^{(j-\frac{1}{2})}$ and $\ddot{u}^{(j)}$ from the previous increment. Thus the explicit integration rule is quite simple; further the use of diagonal element mass matrices enhance computational efficiency as inversion of the mass matrix is central to the computation of initial acceleration as in (10)

$$\ddot{u}^{(j)} = M^{-1}(E^{(j)} - I^{(j)}) \quad (10)$$

The central difference operator requires input of the value of the mean velocity $\dot{u}^{(-\frac{1}{2})}$. The initial values of are set to zero unless they are specified by the user as in (11).

$$\dot{u}^{(+\frac{1}{2})} = \dot{u}^{(0)} + \frac{\Delta t^{(0)}}{2}\ddot{u}^{(0)} \quad (11)$$

Substituting this expression into the updated expression for $\dot{u}^{(j+\frac{1}{2})}$ yields the following definition of $\dot{u}^{(-\frac{1}{2})}$

$$\dot{u}^{(-\frac{1}{2})} = \dot{u}^{(0)} - \frac{\Delta t^{(0)}}{2}\ddot{u}^{(0)} \quad (12)$$

The explicit procedure requires no iterations, thus the explicit finite element dynamic analysis requires less computation cost for each time increment. However, as the central difference operator is only conditionally stable, the increment should be significantly small. The stability limit for the operator is given in terms of the highest Eigenvalue in the system as

$$\Delta t \le \frac{2}{\omega_{\max}}(\sqrt{1+\zeta^2} - \zeta) \quad (13)$$

where ζ is the fraction of critical damping associated with the highest mode. Another conservative estimate of the stable time increment can be as in (14).

$$\Delta t = \min(L_e / C_d) \quad (14)$$

where L_e is the characteristic element dimension and C_d is the current effective dilatational wave speed of the material as defined in (15).

$$C_d = \sqrt{\frac{E(1-\nu)}{\rho(1+\upsilon)(1-2\upsilon)}} \quad (15)$$

ABAQUS/EXPLICIT simulations generally require 10,000 to 1,000,000 increments, but the computational cost per increment is generally relatively small. The process of rail/wheel contact-impact in the vicinity of IRJ is modelled as a high speed impact event in this paper as the process of wheel passage across the IRJ takes only a few milliseconds generating contact forces at frequency of about 500Hz.

4 FINITE ELEMENT MODELLING OF IRJ

4.1 Static-explicit analysis

Prior to impact, the railhead and the wheel must attain steady state of contact. Steady state contact information obtained from static analysis is transferred into explicit dynamics (Fig. 3) (Pang and Dhanasekar, 2006; Zong et al 2010).

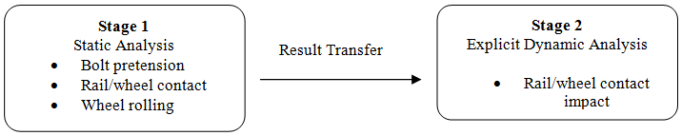

Figure 3: Analysis Stages: Static-Explicit dynamic analysis

A typical insulated rail joint (IRJ) assembly used popularly in the Australian heavy haul rail network is illustrated in Figs 4a and 4c. To maintain the vertical and lateral alignments and the bending stiffness at appropriate levels required for the safe passage of wheels, two lengths of rail are rigidly joined by a pair of supporting plates (fishplates or joint bars) separated by insulating materials. Electrical insulation is also ensured through proper detailing of the insulating material in between the bolt shank and head to the joint bar and rail web.

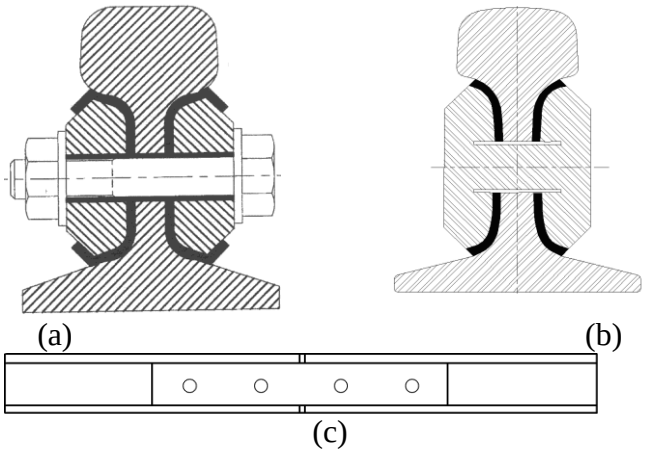

Figure 4: Insulated Rail Joint (a) cross-section (b) simplified model, (c) side view

As the research reported in this paper is focused on the dynamics and failure of the railhead at the wheel contact impact area in the vicinity of the IRJ, the geometry of the IRJ was simplified to just one "part" model by ignoring the interaction between the contact surfaces the rail, the joint bars, the bolts, and the nuts as shown in Fig.4b. This simplified one instance model saves significant computational cost as the need for definition of surface interaction is eliminated. The simplified model has been found quite sufficient for the determination of contact impact force and localised damage of the railhead in the vicinity of the IRJ.

4.2 Wheel rail contact

Proper definition of rail/wheel contact interaction is essential to achieve converged, accurate results within a minimum computational time. A master/slave contact surface method was used for the static (implicit) and the dynamic (explicit) analyses. The wheel surface was considered as the master and the railhead surface was defined as the slave. The contact surface pair was allowed to undergo finite sliding under friction.

For static analysis, hard contact was adopted through the selection of the contact pressure-overclosure relationship and the penalty method was employed to ensure the occurrence of contact. Iterations continued until the solution converged below a threshold value. If a slave node penetrated into the master surface by more than 0.1% of the characteristic interface length, the contact pressure was "augmented" and the process was diverted to a series of iterations until convergence was achieved .

In the dynamic analysis, the penalty contact algorithm first searched for slave node penetrations in the current configuration. Contact forces that were a function of the penetration distance were applied to the slave nodes to oppose the penetration, while equal and opposite forces acted on the master surface at the penetration point. When the master surface was formed by element faces, the master surface contact forces were distributed to the nodes of the faces of the master surface that were penetrated.

At the beginning of the contact analysis, small gaps or penetrations might occur due to numerical round off error, bad assemblies, or inappropriate geometric modelling. Adjusting the initial position of slave contact surface was necessary to eliminate these gaps or penetrations, to overcome convergence problems. In the implicit analysis, an adjustment zone was defined by specifying a depth a. The zone within the distance a in the normal direction from the master surface is termed as the adjustment zone. Any nodes on the slave surface that were within the adjustment zone in the initial geometry of the model were moved precisely onto the master surface. As the adjustment of these slave nodes was carried out as a modification to the initial definition of the geometry of the model, it did not create any additional strain to either of the contacting bodies. When the depth was very large (relative to mesh size), deficient contact condition occurred leading to incorrect stress solution, especially in the area around the contact surface. When the depth specified was too small contact iteration was found to be sensitive to mesh, and convergence problems were encountered. For the current contact between the AS60kg/m railhead and the 460mm radius wheel thread, the depth was set as 0.01 mm. A typical meshed geometry of wheel – railhead is shown in Figure 5.

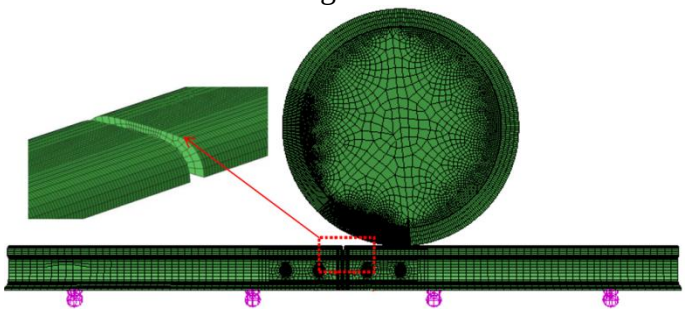

Figure 5: Finite element model

For the regions far away from the contact/stress concentration zone, coarse mesh and 8-node reduced integration element (C3D8R) was used to reduce the model size. While for the regions that undergo contact interaction or high level of stress, refined mesh and 8-node fully integrated element (C3D8) were adopted. To find efficient and accurate element size in this region, a mesh sensitivity analysis was conducted. Figure 6 shows the variations of maximum von Mises stress as the wheel contacting at the original railhead end and computational time with respective to the mesh size. It can be seen that the element size 0.5 is mostly suitable, because the FE model was providing result, while keeping desired efficiency. There were 47303 solid elements for the rail, 53736 elements for the wheel part and 303117 DOFs in the whole system of the most optimal mesh.

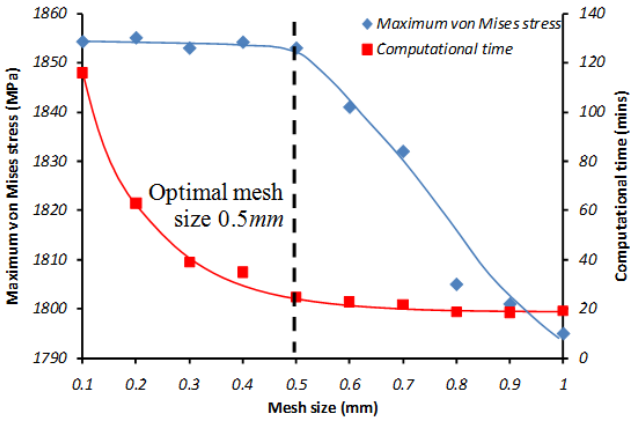

Figure 6: Result of mesh sensitivity study

5 NUMERICAL RESULTS

A 12m long AS60kg/m rail positioned at 1/20 cant was considered. The gap between the ends of the rails along the longitudinal direction (which corresponds to the thickness of the endpost) was set as 10 mm. The sleeper spacing was set as 700mm. A wheel with 460 mm radius was considered rolling/sliding on the top of the railhead. Static load of 150kN was applied to the wheel in the vertical direction. Elastic and plastic properties of the materials used in the analysis are listed in Tables 1 and 2 respectively. Stiffness and damping parameters of the supporting and suspension springs and dashpots are listed in Table 3.

Table 1: Elastic Properties of Materials

Materials	E [MPa]	ν
Rail Steel	210000	0.3
Nylon66	1590	0.39

Table 2: Plastic Properties of Rail Steel

σ_y(MPa)	780	1120	1130
ε_p	0	0.01	0.1

Table 3: Stiffness and Damping Parameters for Supporting and Suspension system

Elastic support system	Suspension system
K_b (MN/m)	K_s (kN/m)
26.8	220
C_b (Ns/m)	C_s (Ns/m)
145	138

Bolt pretension was applied through the internal cross section of the bolt shank that connects the joint bars as detailed in Ding and Dhanasekar [12]. The bolt load Pb was calculated from the bolt torque T, the bolt diameter D and a coefficient Kb (Kb=0.19-0.25) as shown in (16). For the purpose of numerical computation, T, D and Kb were selected as 1050Nm, 24mm, and 0.22 respectively that provided bolt load of 200kN. Initial condition effects were minimised by allowing the wheel to roll a sufficiently long distance prior to impacting at the IRJ. A length of 0.2m was found sufficient for this purpose.

$$P_b = \frac{T}{K_b D} \tag{16}$$

To fully understand the structural response to rail/wheel contact-impact, modal analysis was firstly performed using the IRJ model. Frequencies of the first ten modes of vibration of the IRJ model are presented in Table 4. Some selected modal shapes (the first three and the seventh modes) are shown in Fig.13. The first three modes correspond to translation, rotation, and bending vibrations in the vertical direction. The seventh mode exhibits a very local vibration in the vicinity of the IRJ; the shape of the seventh mode has good resemblance to the deflection of the IRJ under impact, and the frequency of the seventh mode (520Hz) is also close to the frequency of the contact impact force as shown later in this paper. Thus it could be inferred that the impact dynamic response of IRJ might have close correlation to one of its higher modes of vibration; this inference provides some basic principles for developing an appropriate method of dynamic design of the IRJ.

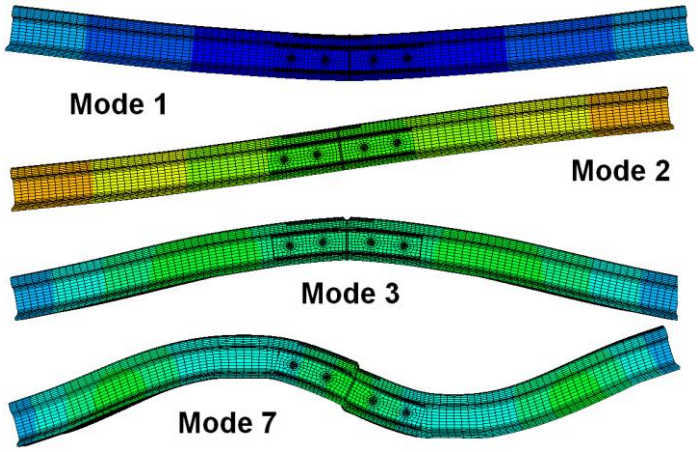

Figure 7: Modal shapes of IRJ

Table 4: Frequencies of the first ten modes of the IRJ

Mode	1	2	3	4	5	6	7	8	9	10
Frequency	116	156	259	298	325	362	520	620	641	756

Special attention was paid to spring support boundary conditions when transferring data from the implicit static analysis to the explicit dynamic analysis. ABAQUS provides the capability to import a deformed mesh and its associated material state; however, the boundary conditions (loading, and contact

interactions) could not be imported and have to be redefined in the explicit model. Although redefining these conditions is straight forward, care should be exercised in retaining the initial forces of the supporting and suspension springs, which have been developed at the end of the steady state static analysis. The initial forces were introduced using the relationship between the spring force F_b and displacement x of springs as follows:

$$F_b = K_s x + F_b^0 \quad (17)$$

where F_b^0 is the spring force obtained in the steady state analysis.

Impact dynamic analysis of the IRJ has provided the railhead/ wheel contact force time history, which is shown in Fig.8. From the figure it can be seen that, at the beginning of the static analysis, the contact force has increased sharply just above 150kN and stabilised to the static wheel load value of 150kN after a short period of one millisecond. As the wheel approached the IRJ, a small drop in the contact force (127kN) occurred due to the local deformation of the edge of the railhead that is affected by the drastic change in the elastic properties between the two interacting materials (rail steel and endpost nylon). Within 0.54 millisecond the contact force increased from 127kN to 174kN (or 37%) indicating the occurrence of the rail/wheel contact-impact. The impact occurred at 7.1 millisecond since the start of the wheel travel. It is believed that the wheel impact at the IRJ is due to the momentary "loss" of contact leading to wheel flight across the end post with the wheel landing on the other edge of the railhead. The exact location of the wheel tending to lose contact and re-landing on the railhead cannot be precisely estimated from the FE model. As 0.54 millisecond of "flight time" of the wheel travelling at 120km/h corresponds to 18.0mm which is larger than the endpost (gap) thickness, it is inferred that the hypothesis of wheel impact in the vicinity of the IRJ is approximately validated. After the impact, the contact force has gradually damped down to the static wheel load level of 150kN. It should also be observed that the post impact history is associated with high frequency noise, which was absent in the pre-impact history of the contact force, which again reinforces that the wheel has actually impacted the forward section of the railhead.

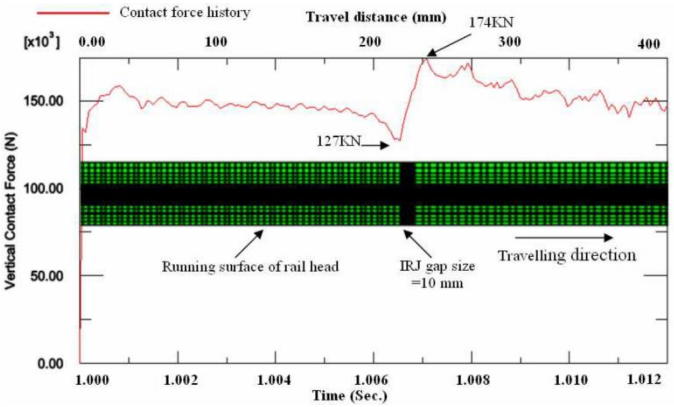

Figure 8: Rail/wheel contact force history (including railhead mesh–plan view)

The kinetic energy history of IRJ is plotted in Figure 9. The very high level kinetic energy was due to the significant contribution from the wagon mass which was 15 ton or 96% of the whole model mass. During the steady state rolling the kinetic energy recorded a gradual reduction with the impact imparting higher levels of kinetic energy. The maximum peak of the kinetic energy occurred at 8.0 millisecond of the travel time, which shows a delay of 0.9millisecond to the time of maximum impact force (Fig. 8). This time delay is in accordance to the theory of impact wave propagation in solids.

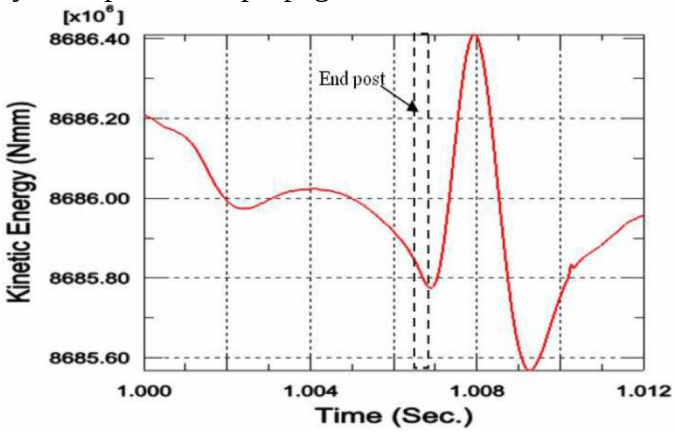

Figure 9: Kinetic energy time history

Although the results presented so far illustrates the occurrence of impact in the vicinity of the IRJ on the railhead near the edge of the rail in a logical manner, to further prove the appropriateness of the FE model for the contact-impact analysis, the endpost material (nylon66) was replaced with the rail steel itself. This modification has effectively removed the joint (discontinuity), with the FE model of the IRJ becoming a rail with no joint; as such no impact should occur. The contact force time history shown in Figure 10 proves that the FE model works well as no impact is found with the contact force remaining at 150kN level (equivalent to static wheel load) throughout the travel.

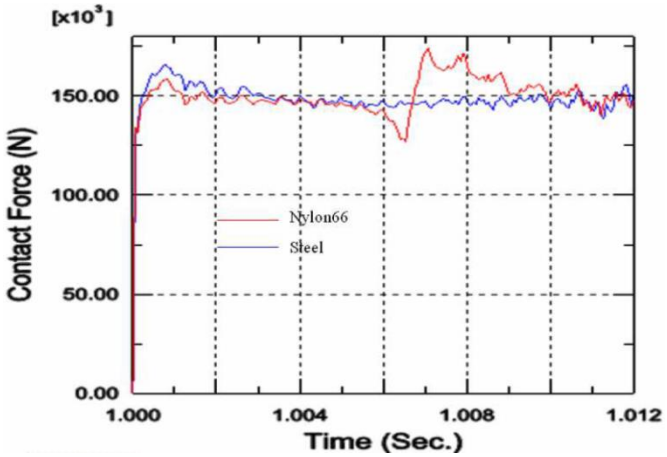

Figure 10: Contact force history of Nylon66 and steel end post material

To infer the effectiveness of gluing the endpost material to the edges of the rail sections, a case was analysed by simply removing the endpost material (simulating simply inserted endpost design of the IRJ, which is also common). The contact impact time history obtained from this analysis is shown in Figure 11. An increased level of impact relative to the glued endpost IRJ is apparent. The damage potential of the increased impact of each wheel passage (185kN – 174kN = 11kN for a static wheel load of 150kN, or 8%) requires further investigation as the economics of gluing the insert against the potential increase in railhead damage requires justification.

Locked wheels due to heavy braking/traction tend to slide and are known as the primary reason for engine burn type of damage even on rails with no joints. The FE model developed was used to analyse the effect of sliding wheels near the IRJ to the contact force history. The IRJ containing glued end post was used for this purpose. Degree of freedom 5 of the wheel was arrested to simulate dragged wheels. The contact force history shown in Fig. 12 illustrates the increase in impact (194kN–174kN=20kN for a static wheel load of 150kN representing 13% increase) force that is significant. It is, therefore, important the operating vehicles ensure good rolling of wheels through application of gentle braking/traction torques.

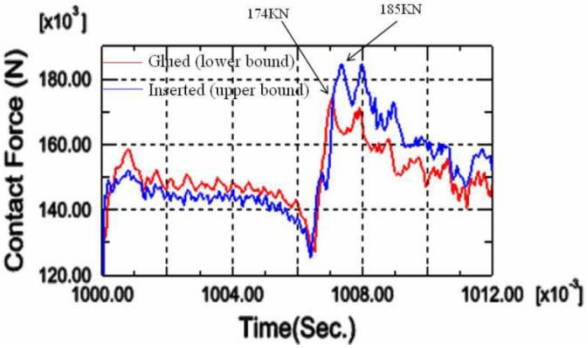

Figure 11: Impact force history with glued and inserted end post

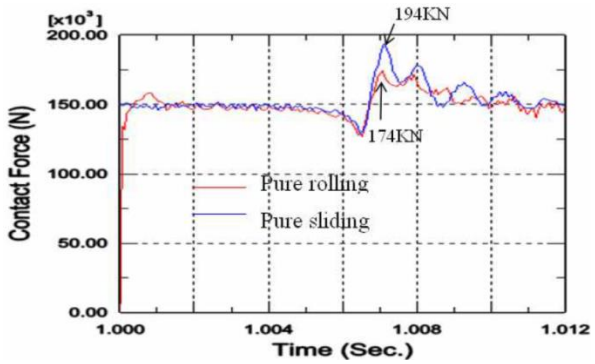

Figure 12: Contact Force Time History due to Rolling Wheel and Sliding Wheel.

The contact pressure on the railhead was monitored throughout the travel of the wheel. Until the wheel approached the discontinuous IRJ, the contact pressure shape was approximately elliptic and the major and minor axes of the ellipse and the magnitude of the maximum contact pressure have been in good agreement with that of the Hertz theory. When the wheel just crossed the IRJ, the shape of the pressure has shown two point contact of the wheel spanning across the IRJ as illustrated in Fig.13. The maximum contact pressure was 1240MPa.

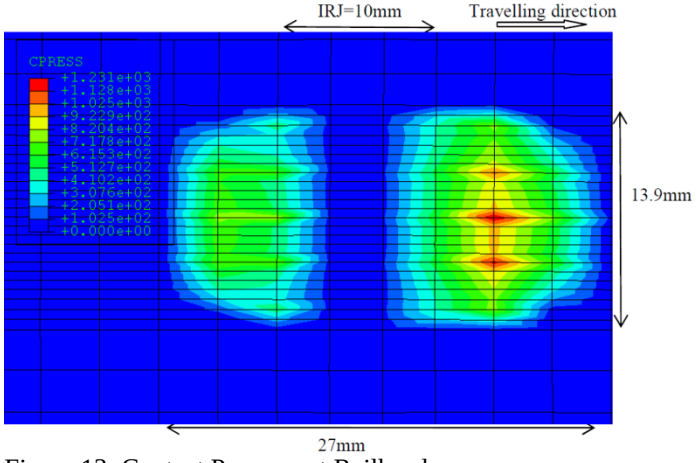

Figure 13: Contact Pressure at Railhead.

6 FIELD EXPERIMENTS

Two strain-gauged IRJs were installed in QR heavy haul network; this paper presents some limited data from one of the test specimens. The IRJ test specimen was factory fabricated with the usual thermal treatment. Strain gauging was performed in coordination with the manufacturer to ensure safe and reliable location of the gauges in the key spot identified by the FE analysis. Only the rail was strain gauged. Strain gauge rosettes were used on both sides of the rail web on both rails that form the IRJ. The two rails were also strain gauged at the foot for the longitudinal strains. A total of fourteen strain channels were thus recorded. A dedicated data acquisition system powered by solar panels was

housed at the site. The IRJ specimens were statically loaded to ensure the repeatability of the strain gauge readings prior to site installation. A photograph of the test site is shown in Figure 14. As the objective of the test was to assess the mechanical integrity of the IRJ, the rails were electrically bonded. Staff visited the site on a weekly basis for down loading the data and general check-up and cleaning operation including photographing. A photo of the top view of the IRJ is shown.

(a) (b)

Figure 14: Field experimentation of IRJ: (a) field setup; (b) top view of IRJ.

6.1 Strategies for strain recording

As the wheel passage across the joint is an event that lasts for only a very short period (for example for 80km/h operation, the wheel would take 0.45 milliseconds to cross a nominally 10mm thick joint), data must be recorded at a very high frequency. Data recording was therefore set at 20,000 data points per second. As this high sampling rate was only required during train passage, an ultrasonic object detector was used to trigger the data recorder. When no trains were present, the recorder recorded the strains at the rate of one data point per five minutes. The time and temperature (ambient) readings were also recorded at this rate. The corridor services mixed traffic. As the project was focussed on the response of IRJ to heavy axle loaded (Coal) traffic, strategies were required to sort out the data corresponding to the loaded coal trains. Several strategies were formulated based on the information on train composition, traffic data and the strain signatures. A full description of all strategies is beyond the scope of this paper. Some idea could however be presented with reference to Figure 15.

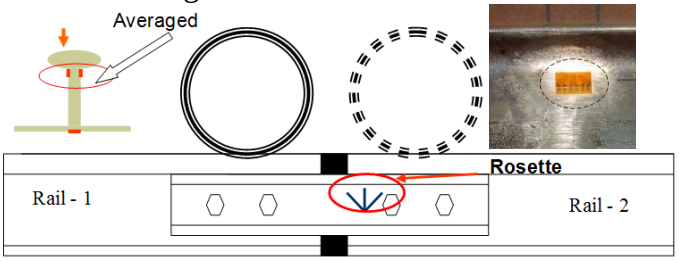

Figure 15: Averaged strain analysis method

First as the wheels do not run symmetric to the vertical axis of the rail, the strain components measured from the opposite faces of the rail web have been averaged. A typical vertical strain signature is shown in Figure 16. Each spike corresponds to the averaged vertical strain at one of the rosette locations for 10 seconds of train travel (200,000 data points). The average strains were of the order 500 microstrain. Each spike in the figure corresponds to one wheel passage across the joint (also the gauge location).

Second, from the shape of the vertical normal strain signature (Figure 17), the direction of travel has been identified. The figures show the zoomed version of the tip of a spike in Figure 16. Figure 17a shows the vertical strain signature obtained from the rosette attached to Rail 2 for wheels travelling from left to right. It can be seen that these wheels first cross the joint (causes impact at Rail 1) and then roll over the gauge point. Whilst the wheels travelling from right to left crosses the gauge first and then impacts the Rail 2; therefore the impact is not explicitly captured by the rosette in Rail 1. Using this information, the direction of travel of the wheel (train) was deduced.

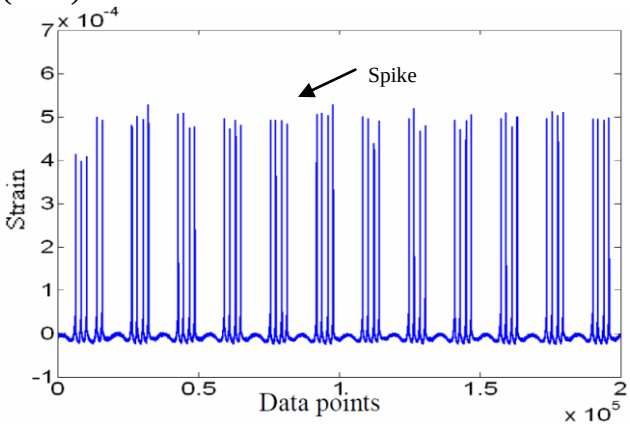

Figure 16: A typical averaged vertical strain history.

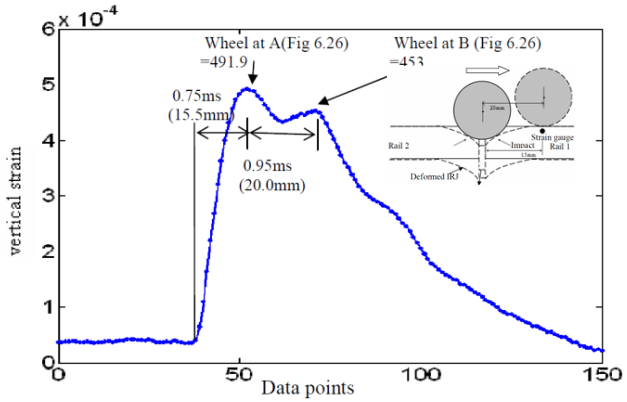

(a) From left to right

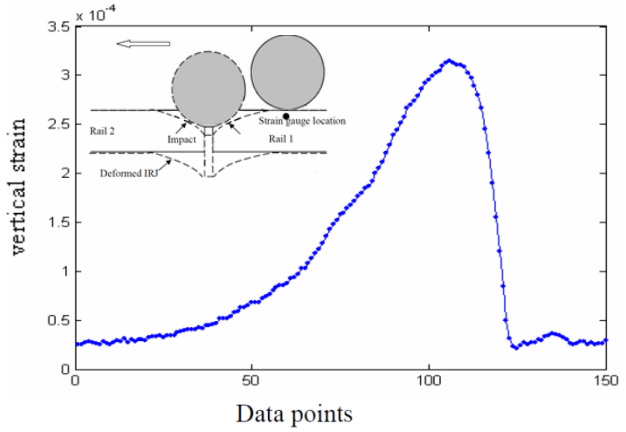

(b) From right to left

Figure 17: Illustration of strain gauge data at different travel directions

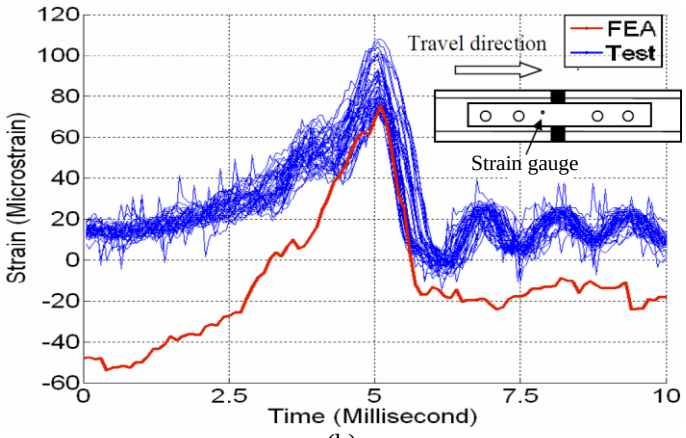

(b)

Figure 18: Comparison of strains between FE model and field data.

Third, using the details of the composition of the trains and the design of bogies (for example axle spacing), it was possible to assess the speed of travel of the wheels. The axle load and speed data were vital for the finite element analysis input. With these input data, vertical strain time series could be predicted by the developed FE model (Section 6), which in turn could be validated using the strain signatures from the field.

6.2 Validation of FE model using field data

A comparison of the FE predicted vertical strain signatures for both the loaded and empty wagon cases are shown in Figures 18. Given the complexities of the problem and the limitations of both the FE and experimental dataset, it is believed that the comparison is quite good.

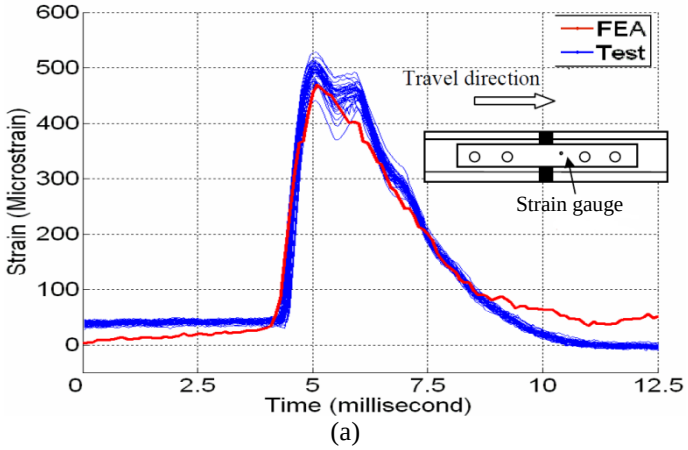

(a)

The good comparison provides confidence in the contact-impact force time series predicted by the FE model. The 'validated' FE model could be run for a number of scenarios of operational parameters (axle loads, speeds), maintenance regimes (wheel condition, railhead condition) and tribological parameters (contact surface roughness, friction coefficients), and a range of contact-impact forces and the corresponding state of (elastic) strain at key locations could be determined. These strain–contact force 'plots' could be used as calibration charts in the field for inferring contact-impact forces from simple strain gauge data sets at key locations. Such strain gauge data need not be collected continuously; random checks of strain levels would suffice making the method economical from a data overloading perspective.

Impact forces are the major contributing parameter for low cycle fatigue dominated ratchetting type of failure. Therefore predicted levels of the contact forces would form a sound basis for the determination of the life of the joints. Life of materials and structures subjected to variable amplitude low cycle fatigue loading is well researched area. Although the results are not conclusive, once the load cycles are determined with confidence (as reported in this paper) one can use the literature base for working out the life of the joints. Work is ongoing for predicting the failure of IRJs dominated by metal flow across the insulator; results of which can be reported in the forthcoming conferences.

7 CHARACTERISATION OF MATERIALS IN PLASTIC ZONE OF INSULATED RAIL JOINTS

Common approaches to the experimental characterisation of the plastic zones of rail steels include: optical and electron microscopy investigations, applied to bulk rails by Osterle et al. (2001) and Zhang et al

(2006) and to rail ends by Rathod et al. (2012); analysis of surface texture development (Satoh and Iwafuchi (2005)); localised mechanical property evaluation by hardness, wear, tensile and/or fatigue testing (Zhang et al. 2006); investigations of variations in accumulated stress using x-ray or synchrotron diffraction techniques (Osterle et al. (2001)), neutron diffraction study of bulk rail and rail ends (Luzin et al. (2012) and Luzin et al. (2013)); and by magnetic stress measurements (Lo et al. (2010)). The determination of plastic properties of rail material using any of the current method, particularly close to the rail surface, is complex due to the variety of microstructures present at difference length scales below the rail surface.

7.1 Microstructures

Metal movement over the insulating gap can either be continuous, resulting from sub-surface flow, or discrete, for example, resulting from displacement of fractured rail over the gap by a mechanism such as spalling. Figure 19, extracted from Rathod et al. (2012) and Luzin et al., (2013), shows damaged ex-service IRJ rail ends after severe deformation in the head hardened region. The low magnification macro, Fig 19 (a) shows squat formation over the insulating gap rendering the IRJ unsafe. The fracture surface below squats (Fig 19 (b)) typically extends around 3-15 mm below the rail surface. Reflected light microscopy (Fig 19 (c) and (d)) and Scanning electron microscopy (Fig 19 (e) and (f)) reveal a highly deformed layer near the surface, the depth of this layer increasing with increasing service life. Such layers are generally too complex or thin to perform mechanical tests. In fact, the very top surface layer of severely deformed pearlitic rail steel is a nanostructure, often revealed as a white etching layer in optical micrographs, and has been found to comprise severely deformed pearlite lamellae, nanocrystalline martensite, austenite and cementite. Below the deformed regions the bulk microstructures appeared free from any significant deformation, however, transmission electron microscopy generally reveals significant accumulation of defects and, as described in the next paragraph, there is also significant accumulation of residual stresses.

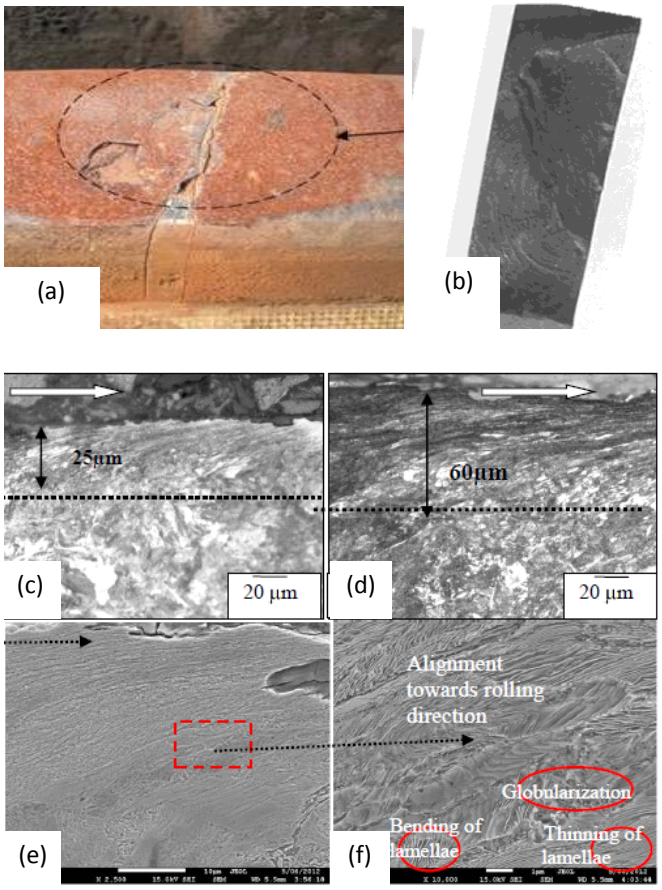

Figure 19 Damage to an IRJs in the vicinity of the insulating gap (from [38] and [40]); macros of squats (a) and (b); surface damage in longitudinal direction after moderate (c) and severe (d) damage (arrow indicates rolling direction); SEM images of damaged surface at (e) low and (f) high magnification.

7.2 Neutron diffraction

The determination of the complex residual stresses developing near and below the surface of the railhead, particularly in the vicinity of the rail ends of IRJs can assist in the validation of models and also help us better understand microstructural degradation associated with metal flow, spalling and rail head checking fatigue cracks. Residual stresses within the rail result in crystal lattice distortions manifest, for the case of head hardened pearlitic rail steel, as a detectible shift in the (211) atomic planes of the alpha Fe phase within the pearlitic matrix. While x-rays can only enter steel to a depth of around 1 micrometer neutrons can penetrate depths of over 10 mm and for this reason neutron diffraction represents has become a well-established approach for the determination of residual stresses inside bulk steel samples.

In the current series of experiments, samples of rail end were sectioned in transverse and longitudinal directions at 2, 4 and 6mm from the top rail surfaces and differential residual stress measurements were obtained from individual gauge volumes near

the rail end surface of 3mm×3mm×3mm obtained. To speed up processing times 5 mm thick electric discharge machined slices were used for the analyses, the cost of sample sectioning being a loss of data for the plane normal component of residual stress and a the partial loss for other stress components. However, because results for both the original as-manufactured and the ex-service rail components can be compared quite useful information on localised stress accumulation is obtained. Figure 19, extracted from Luzin et al. (2013), shows differential maps of the longitudinal stress tensor component distributions for longitudinal slices for an as-manufactured rail end (top), an electric discharge machined (EDM) cut ex-service rail end (centre) and a rail end from a severely damaged IRJ (lower left), the top left corner being the surface of the rail end abbuting the insulating gap. Notably, the geometry of the localised subsurface compressive zone (blue) changes shape in the vicinity of the rail end top surfaces, for the damaged IRJ rail end. It is interesting to note that position this compressive zone away from the rail end, around 5-10 mm below the rail surface, corresponds to depths of typical head checks and squats commonly observed in damaged rail.

Ideally, a full neutron diffraction residual stress analysis of IRJs would include determination of residual stress in other IRJ components. To address this, a series of experiments is currently underway at the Australian Nuclear Sceince and Technology Organisation in order to investigate stress accumulation in track web and fishplates in as-manufactures and ex-service components (Figure 20).

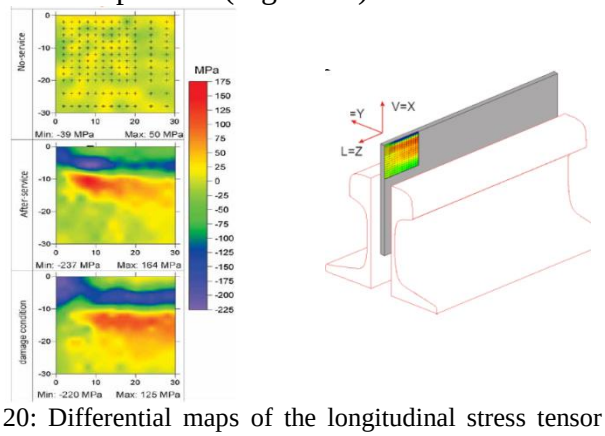

Figure 20: Differential maps of the longitudinal stress tensor component distributions for the longitudinal slices for as-manufactured rail end.

8 CONCLUSIONS

A three dimensional implicit-explicit finite element model coupled with submodelling technique has been described for simulations of rail/wheel dynamic contact impact and railhead damage in the vicinity of IRJ. The model has shown that impact occurs even when new wheels pass over the new, well installed IRJs with no dip. From the results obtained, it was shown that the frequency of the impact force for the type of wheel-IRJ system considered has been dominated by its seventh mode. It has also been shown that the characteristics of the insulation materials have direct influence on the impact force factors; the closer these material properties are to rail steel, the lower the contact impact forces are.

Nonlinear elasto-plastic static analysis of submodelling in the vicinity of the IRJ is effective in determining the localised railhead damage. The damage occurs in the form of both closing the gap (and reducing the endpost thickness) and forming a vertical dip. This study provides a useful method for further research on fatigue analysis of railhead near IRJ; the ongoing research including field experimentation of IRJ is promising.

In addition, the residual stress of the railhead steel slides extracted from the pre-service, post-service and damaged rail end samples are analysed using Neutron diffraction techniques. The result has demonstrated that the free edge of the joint gap has drawn the significant residual stress concentration at the top corner of the railhead end, resulting in early material failure at the joint. Further comprehensive study on the micro-level behaviours of the railhead at the joint is ongoing.

Acknowledgements

This work was funded by the CRC for Rail innovations (R3.100). The support of Tao Pang, former researcher at Central Queensland University, Ross Gambling, Network Access, QR, Rockhampton and Tim McSweeney, formerly track systems manager, QR and current research support officer, CRE at many stages of this ongoing project are thankfully acknowledged. The support of Paul Boyd (CQU), Chandrahas Rathod (UoW) and Dr. Vladimir Luzin (ANSTO) are also sincerely thanked.

REFERENCES

Davis DD, Akhtar MN. (2005), Improveing the performance of bonded insulated joints, Railway Track & Structures, TTCI R&D; 2005;14-7.

Newton SG. Clark RA. An investigation into the dynamic effect on the track of wheelflats on railway wagon. Journal of Mechanical Engineering and Science, 1979;21; 287-97.

Kerr AD, Cox JE. Analysis and test of bonded rail joints subjected to vertical wheel loads, Int. J. Mech. Sci, ASME. 1999;41;1253-72.

Jenkins, HH. Stephenson, JE. Clayton, GA. Morland, GW. Lyon D. The effect of track and vehicle parameters on

wheel/rail vertical dynamic forces. Railway Engineering Journal 1974;3;2-16.

Steenbergen, M.J.M.M. Modelling of wheel and rail discontinuities in dynamic wheel-rail contact analysis. Int J of Vehicle System Dynamics. 2006; 44(10); 763-87.

Chen YC. Kuang JH. Contact stress variations near the insulated rail joints. Proceedings of the Institute of Mechanical Engineers, Part F, Journal of Rail and Rapid Transit. 2002;216;265-74.

Chen YC. Chen LW. Effect of insulated rail joint on the wheel/rail contact stress under the condition of partial slip. Wear, 2006, 260, 11-12; 1267-73.

Wen Z. Jin X. Zhang W. Contact-impact stress analysis of rail joint region using the dynamic finite element method, Wear, 2005;258;1301-09.

Heinsch M. 2004. Improving rail durability and life. Int Railway Journal, XLIV(2); 13-15.

Marich S. 2006. Practical/ realistic implementation of wheel-rail contact technologies – the Australian experience. Proc. 7th Int Conf Contact Mechanics and Wear of Rail/Wheel Systems, Brisbane, 3-21.

Higgins RL, Otter DE, Martin RW, Irani FD, El-Sabaie MA, Vandeberg RM, Jackson R and Ring ME. 1996. Instrumented wheelset system. US Patent Number 5492002, http://www.patentstorm.us/patents/5492002.html

Jonsson J., Svensson E. and Christensen JT. 1997. Strain gauge measurement of wheel-rail interaction forces. Journal of Strain Analysis, 32(3): 183-191.

Pang, T. & Dhanasekar, M. (2006). Dynamic finite element analysis of the wheel-rail interaction adjacent to the insulated rail joints, Proceedings of 7th international conference on contact mechanics and wear of rail/wheel systems, 24-27 September,

Zong, Nannan, Dhanasekar, Manicka, Bayissa, Wirtu, & Boyd, Paul (2010) Study of wheel-rail impact at insulated rail joint through experimental and numerical methods. In Key Technologies of Railway Engineering-High-speed Railway, Heavy Haul Railway and Urban Rail Transit, China Railway Publishing House, Beijing Jiaotong University, Beijing, pp. 356-360.

Zong, Nannan & Dhanasekar, Manicka (2012) Minimization of railhead edge stresses through shape optimization. Engineering Optimization, In press.

Osterle, Rooch H, Pyzalla A, Wang L, (2001) Investigation of white etching layers on rails by optical microscopy, electron microscopy, X-ray and synchrotron diffraction, Materials Science and Engineering A303; 150–157.

Zhang HW, Ohsaki S, Mitao S, Ohnumaa M. Honoa K. (2006) Microstructural investigation of white etching layer on pearlite steel rail, Materials Science and Engineering A 421; 191–199.

Rathod C, Wexler D, Chandra T and Li H. (2012) Microstructural characterisation of railhead damage in insulated rail joints, Materials Science Forum 706-709; 2937-2942.